RESEARCH BRIEF

Histone H3.3 Mutations Drive Pediatric Glioblastoma through Upregulation of MYCN

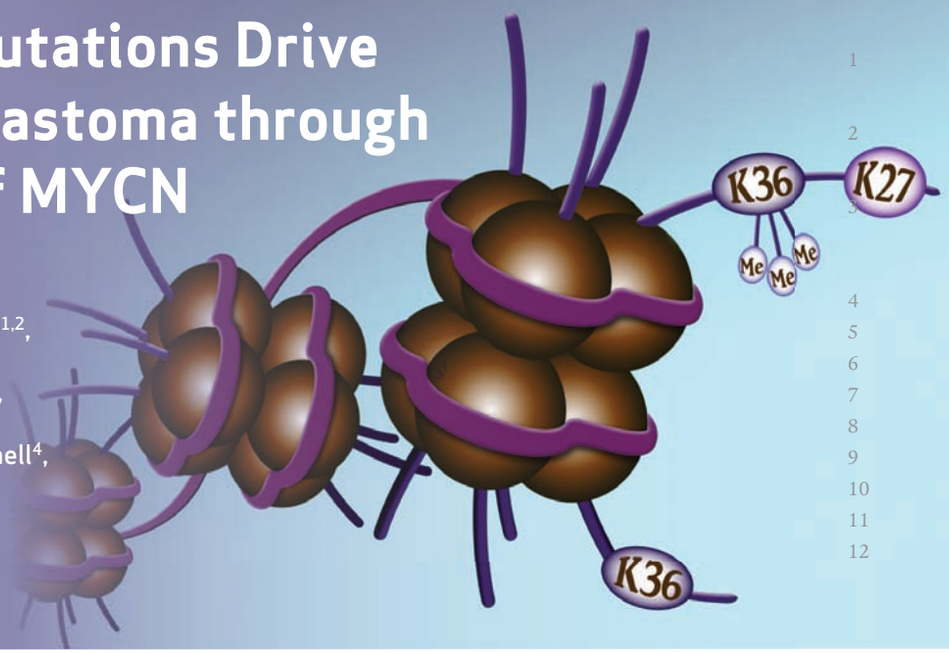

Lynn Bjerke[1,2], Alan Mackay[1,2], Meera Nandhabalan[1,2], Anna Burford[1,2], Alexa Jury[1,2], Sergey Popov[1,2], Dorine A. Bax[1,2], Diana Carvalho[1,2,6,7], Kathryn R. Taylor[1,2], Maria Vinci[1,2], Ilirjana Bajrami[1,3], Imelda M. McGonnell[4], Christopher J. Lord[1,3], Rui M. Reis[7,8], Darren Hargrave[5], Alan Ashworth[1,3], Paul Workman[2], and Chris Jones[1,2]

ABSTRACT

Children and young adults with glioblastoma (GBM) have a median survival rate of only 12 to 15 months, and these GBMs are clinically and biologically distinct from histologically similar cancers in older adults. They are defined by highly specific mutations in the gene encoding the histone H3.3 variant *H3F3A*, occurring either at or close to key residues marked by methylation for regulation of transcription—K27 and G34. Here, we show that the cerebral hemisphere-specific G34 mutation drives a distinct expression signature through differential genomic binding of the K36 trimethylation mark (H3K36me3). The transcriptional program induced recapitulates that of the developing forebrain, and involves numerous markers of stem-cell maintenance, cell-fate decisions, and self-renewal. Critically, *H3F3A* G34 mutations cause profound upregulation of *MYCN*, a potent oncogene that is causative of GBMs when expressed in the correct developmental context. This driving aberration is selectively targetable in this patient population through inhibiting kinases responsible for stabilization of the protein.

SIGNIFICANCE: We provide the mechanistic explanation for how the first histone gene mutation in human disease biology acts to deliver MYCN, a potent tumorigenic initiator, into a stem-cell compartment of the developing forebrain, selectively giving rise to incurable cerebral hemispheric GBM. Using synthetic lethal approaches to these mutant tumor cells provides a rational way to develop novel and highly selective treatment strategies. *Cancer Discov; 3(4); xxx–xxx. ©2013 AACR.*

INTRODUCTION

The clinical and molecular differences observed in glioblastoma (GBM) of children and young adults compared with the more common, histologically similar lesions in older adults is strongly suggestive of a distinct underlying biology (1). The identification of unique and highly specific mutations in the gene encoding the histone H3.3 variant *H3F3A* in GBM of

Authors' Affiliations: [1]Divisions of Molecular Pathology, [2]Cancer Therapeutics, and [3]Breast Cancer Research, The Institute of Cancer Research; [4]Royal Veterinary College; [5]Great Ormond Street Hospital, London, United Kingdom; [6]University of Coimbra, Coimbra; [7]ICVS, University of Minho, Braga, Portugal; and [8]Molecular Oncology Research Center, Barretos Cancer Hospital, Barretos SP, Brazil

Corresponding Author: Chris Jones, Glioma Team, Divisions of Molecular Pathology and Cancer Therapeutics, The Institute of Cancer Research, Sutton, Surrey, SM2 5NG, United Kingdom. Phone: 44-020-8722-4416; Fax: 44-020-8722-4321; E-mail: chris.jones@icr.ac.uk

Note: Supplementary data for this article are available at Cancer Discovery Online (http://cancerdiscovery.aacrjournals.org/).

doi: 10.1158/2159-8290.CD-12-0426

children and young adults has recently provided definitive proof of this hypothesis (2). However, a mechanism was lacking for how mutations at or close to key residues associated with posttranslational modification of the histone tail led to tumorigenesis.

We have sought to address this by examining how the differences in clinical presentation, anatomic location, and gene expression associated with the different *H3F3A* mutations are manifested. By exploiting the only known G34-mutant model system, we show that differential binding of the H3K36 trimethyl mark underpins these processes and identify MYCN as the oncogenic driver during forebrain development, providing a novel avenue for targeted therapy in children with these tumors.

RESULTS

Initial evidence suggested a distinct gene expression signature associated with mutations at the K27 (lysine to methionine, K27M) versus G34 (glycine to either arginine, G34R, or valine, G34V) residues (2). We validated these data by identifying differential expression patterns for mutations with G34 versus K27 mutations in 2 independent datasets for which mutation data were either publicly available or were ascertained in our laboratory (refs. 2, 3; Fig. 1). In both instances, highly significant differential gene expression was noted between G34-mutant tumors and K27 or wild-type cases (Fig. 1A and C), which was consistent across the datasets as assessed by gene set enrichment analysis (GSEA; Figs. 1B and D) with enrichment scores (ES) of 0.833 to 0.943 and P (family-wise error rate; FWER) and q (false discovery rate; FDR) values of 0.0 to 0.04. Given the considerable overlap in gene expression signatures between studies, we subsequently utilized an integrated dataset (Supplementary Table S1), where hierarchical clustering resolved G34- and K27-mutant tumors from a more heterogeneous wild-type subgroup (Fig. 1E), confirmed by k-means consensus clustering (Fig. 1F). These subgroups also showed important clinical differences, as previously described (2), with K27-mutant tumors arising in younger children (peak age 7 years; $P = 0.0312$, t test; Fig. 1G) and having a worse clinical outcome ($P = 0.0164$, log-rank test; Fig. 1H) compared with G34 tumors (peak age 14 years) and *H3F3A* wild-type. There were no significant transcriptional or clinicopathologic differences between G34R and G34V tumors, although a lack of samples of the latter ($n = 2$) precludes robust analyses.

To understand the functional significance of *H3F3A* mutations in cerebral hemispheric tumors, we turned to a well-characterized (4) model of pediatric GBM, the KNS42 cell line, which was derived from a 16-year-old patient and harbors the G34V mutation (Fig. 2A). In contrast to the reported data in a single pediatric GBM sample with G34R (2), KNS42 cells did not show increased levels of total histone H3K36 trimethylation compared with a panel of *H3F3A* wild-type pediatric glioma cells (Fig. 2B, Supplementary Fig. S1). KNS42 cells harbor a nonsynonymous coding change of *ATRX* (Q891E) that appears in the single-nucleotide polymorphism databases (rs3088074), and Western blot analysis shows no diminution of protein levels. As ATRX is a known chaperone of histone H3.3 to the telomeres, a wild-type protein would not be expected to convey the alternative lengthening of telomeres (ALT) phenotype, as observed (Supplementary Fig. S2); however, this ought not play a significant role in gene transcription as deposition of H3.3 in euchromatin is carried out by alternative chaperones such as HIRA.

We conducted chromatin immunoprecipitation linked to next-generation whole genome sequencing (ChIP-Seq) for H3K36me3 to test the hypothesis that, rather than total H3K36me3, the G34V mutation may instead result in differential binding of the trimethyl mark throughout the genome. Compared with *H3F3A* wild-type SF188 pediatric GBM cells, H3K36me3 was found to be significantly differentially bound in KNS42 cells at 5,130 distinct regions of the genome corresponding to 156 genes (DESeq $P < 0.05$, overall fold change >2, contiguous median coverage >2; Supplementary Table S2). These observations were not due to differential gene amplification, as concurrent whole genome DNA sequencing showed that these bound genes were not found in regions on cell line-specific copy number alterations (Fig. 2C; Supplementary Fig. S3 and Supplementary Table S2). As the H3K36 residue is regarded as an activating mark for gene expression (5), we concurrently conducted ChIP-Seq for RNA polymerase II to produce a read out of transcriptional activity, and observed a significant correlation between H3K36me3 and RNA polymerase II binding for the 156 differentially bound genes ($R^2 = 0.923$, $P < 0.0001$; Fig. 2D). By integrating the H3K36me3 and RNA polymerase II data, we derived a ranked list of differentially trimethyl-bound and expressed genes (Fig. 2E). Interrogating this ranked list using our integrated pediatric GBM expression dataset showed highly significant enrichment for G34-associated gene signatures in the differentially bound and expressed genes in G34-mutant KNS42 cells (ES = 0.84–0.86, FWER $P = 0.02$–0.03; FDR $q = 0.03$–0.04; Fig. 2F).

To investigate the functions of the transcriptional programs targeted by this novel mechanism, we conducted gene ontology analysis of the differentially bound and expressed genes. These data revealed highly significant enrichment of the processes involved in forebrain and cortex development, as well as differentiation of neurons and regulation of cell proliferation (Fig. 2G). We identified a subset of 16 genes to be part of the core enrichment group showing significant overlap between G34-mutant pediatric GBM specimens and transcription driven by differential binding of H3K36me3 in KNS42 cells (Supplementary Table S3). By mapping the expression of these genes to published signatures of restricted spatiotemporal areas of brain development (6), we noted highly elevated levels at embryonic and early fetal time-points, which rapidly tailed off through mid-late fetal development and postnatal and adult periods (Fig. 2H). Expression of the G34 core enrichment genes was particularly pronounced in the early fetal amygdala, inferior temporal cortex, and the caudal, medial, and lateral ganglionic eminences (Fig. 2H). Developmental expression patterns of G34 mutation-associated genes were in contrast to those observed with K27 mutation signatures derived from pediatric GBM specimens, which correlated with those of the embryonic upper rhombic lip, early-mid fetal thalamic, and cerebellar structures, and peaked during the mid-late fetal period (Supplementary Fig. S4).

Specifically, the G34 mutation drives expression of numerous highly developmentally regulated transcription factors, including as an exemplar *DLX6* (distal-less homeobox 6), a homeobox transcription factor which plays a role in neuronal differentiation in the developing forebrain (7). The highly significant

[Q7]

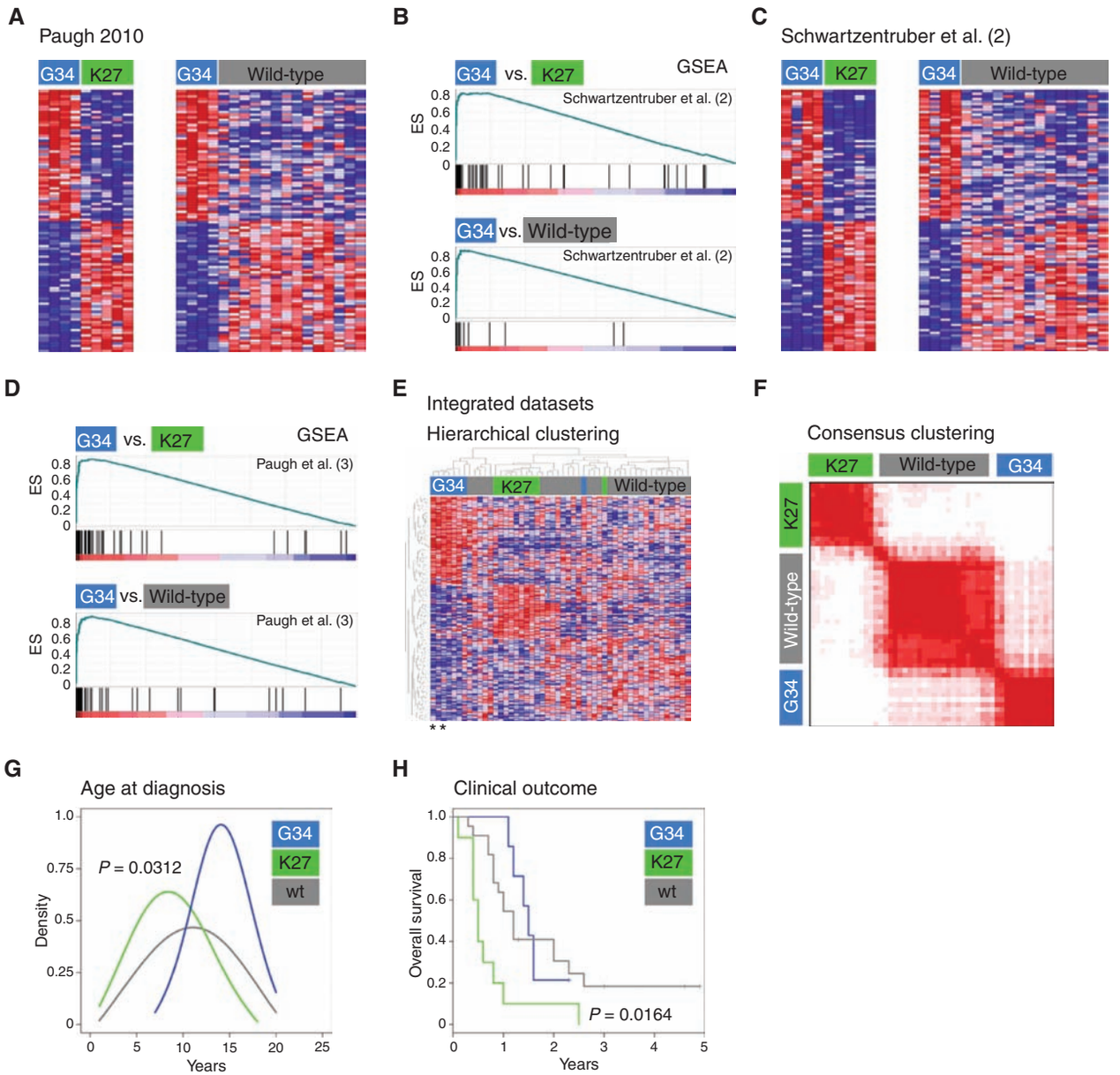

[Q8]

Figure 1. Distinct molecular and clinical correlates of *H3F3A* mutation subgroups. **A,** heatmap representing differential gene expression signatures between G34 versus K27, and G34 versus wild-type, pediatric GBM specimens identified by Paugh and colleagues (3). Top 100 differentially expressed genes are shown for each comparison. **B,** gene set enrichment analysis (GSEA) for differential gene expression signatures identified by Schwartzentruber and colleagues (2) versus those from Paugh and colleagues (3). Top, G34 versus K27: enrichment score (ES) = 0.833, *P* [family-wise error rate (FWER)] = 0.0, *q* [false discovery rate (FDR)] = 0.0. Bottom, G34 versus wild-type: ES = 0.94, FWER *P* = 0.0, FDR *q* = 0.0. **C,** heatmap representing differential gene expression signatures between G34 versus K27, and G34 versus wild-type, pediatric GBM specimens from (2). Top 100 differentially expressed genes are shown for each comparison. **D,** GSEA for differential gene expression signatures identified in (3) versus those in (2). Top, G34 versus K27: ES = 0.88, FWER *P* = 0.03, FDR *q* = 0.04. Bottom, G34 versus wild-type: ES = 0.90, FWER *P* = 0.0, FDR *q* = 0.0. **E,** hierarchical clustering of the integrated gene expression datasets, highlighting specific clusters of G34- and K27-mutant tumors, distinct from a more heterogeneous group of wild-type cases. G34V tumors are represented by asterisks. **F,** K-means consensus clustering finds the most stable number of subgroups to be 3, marked by *H3F3A* mutation status. **G,** K27- and G34-mutant pediatric GBM in our integrated dataset have distinct age incidence profiles, with K27 tumors peaking at 7 years in contrast to G34 at age 14. The 2 G34V tumors were diagnosed at age 14 and 20. **H,** Kaplan–Meier plot for overall survival of pediatric patients with GBM stratified by *H3F3A* status. K27-mutant tumors have significantly shorter survival than G34 (*P* = 0.0164, log-rank test). A single G34V case for which data were available had an overall survival of 1.4 years. wt, wild-type.

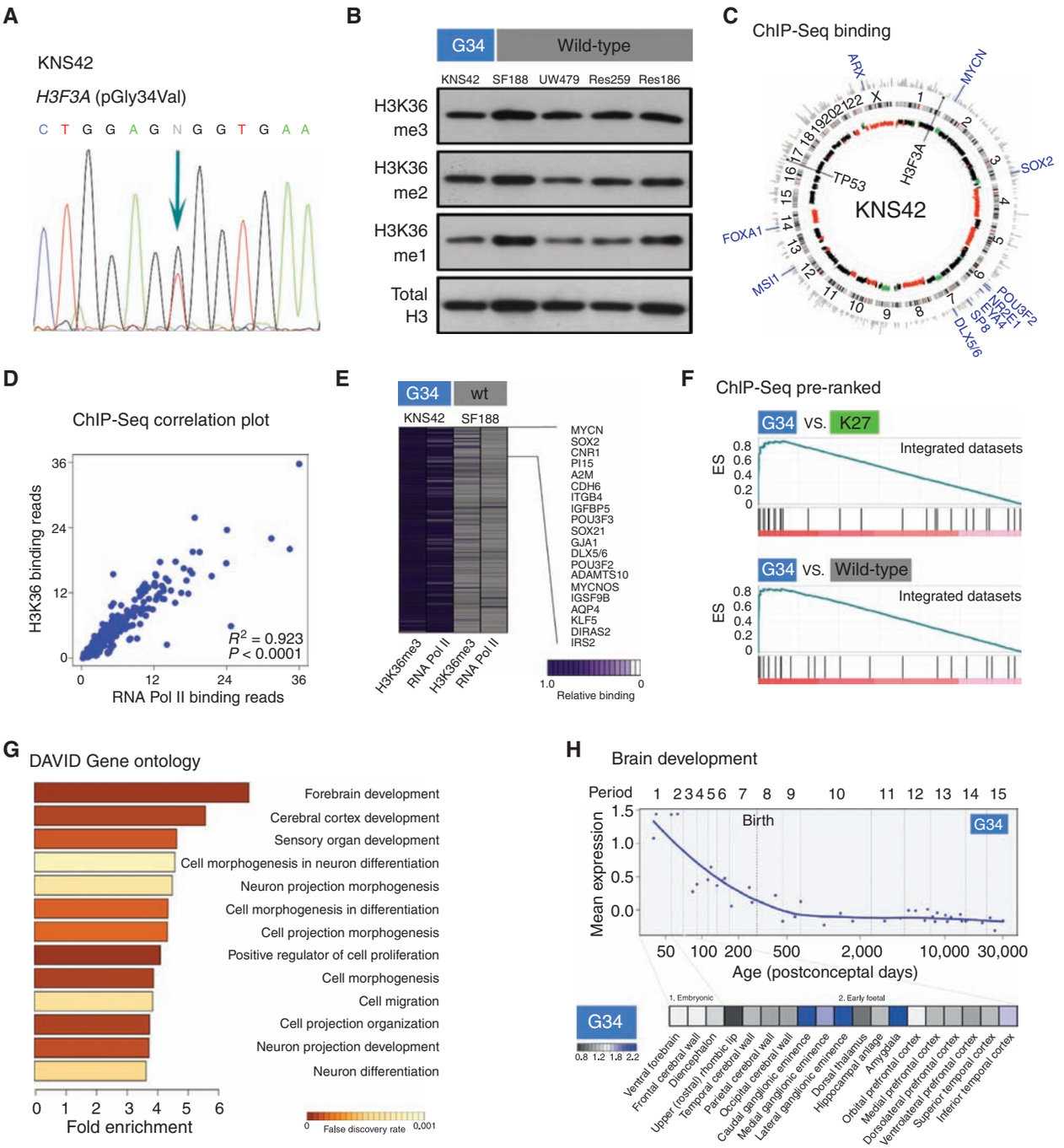

Figure 2. Differential binding of H3K36me3 in G34-mutant KNS42 cells drives pediatric GBM expression signatures. **A,** Sanger sequencing trace for KNS42 pediatric GBM cells reveals a heterozygous c.104G>T p.(Gly34Val) *H3F3A* mutation. **B,** Western blot analysis for mono-(me1), di-(me2), and tri-(me3) methylated histone H3 in G34-mutant KNS42 and wild-type (wt) pediatric glioma cell lines. Total H3 is used as an extracted histone loading control. **C,** Circos plot representing the KNS42 genome, aligned with chromosomes 1 to X running clockwise from 12 o'clock. Outer ring, H3K36me3 ChIP-Seq binding. Gray, all binding; blue, differential binding in KNS42 versus SF188. Selected differentially bound developmental transcription factors and pluripotency genes are labeled. Inner ring, DNA copy number. Green points, copy number gain; black points, normal copy number; red points, copy number loss. Single base mutations in selected genes (*H3F3A*:G34V and *TP53*:R342*) are labeled inside the circle. **D,** correlation plot of RNA polymerase II versus H3K36me3 for 65 differentially trimethyl-bound regions by ChIP-Seq in KNS42 cells. $R^2 = 0.66$; $P < 0.0001$. **E,** heatmap representing a ranked list of differentially bound H3K36me3 and RNA polymerase II in G34V KNS42 versus wild-type SF188 cells, with top 20 genes listed. **F,** GSEA for preranked differentially bound genes identified in ChIP-Seq versus those in the integrated gene expression datasets. Top, G34 versus K27: ES = 0.86, FWER $P = 0.03$, FDR $q = 0.03$. Bottom, G34 versus wild-type: ES = 0.84, FWER $P = 0.02$, FDR $q = 0.04$. **G,** DAVID gene ontology analysis for preranked list of differentially bound genes identified in ChIP-Seq. Fold enrichment of processes are plotted and colored by FDR *q* value. **H,** top, mean expression of the G34 core enrichment signature in a temporal gene expression dataset of human brain development. Period 1, embryonal; periods 2–7, fetal; periods 8–12, postnatal; periods 13–15, adulthood. Bottom, heatmap representing spatial differences in G34 core enrichment signature expression in structures within embryonic and early fetal development, with highest levels mapping to the ganglionic eminences and amygdala.

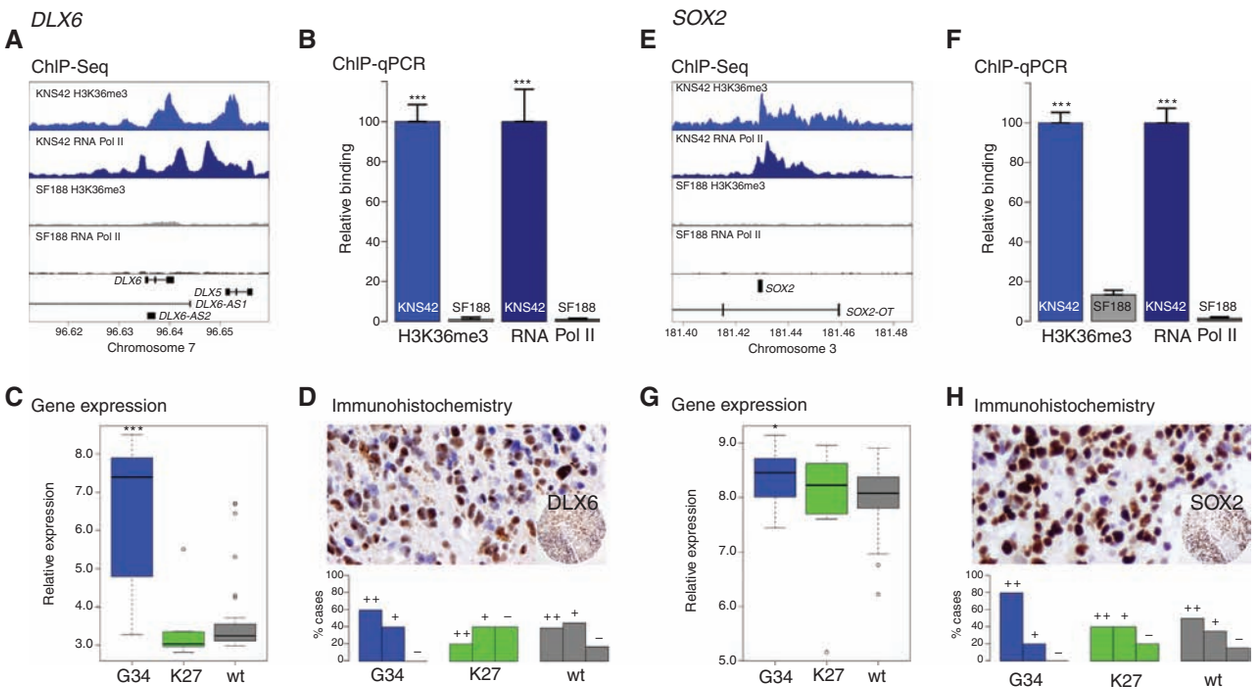

Figure 3. G34 induces a transcriptional program linked to forebrain development and self-renewal. *DLX6*: **A,** ChIP-Seq of H3K36me3 and RNA polymerase II binding for G34-mutant KNS42 (blue) and wild-type (wt) SF188 cells (gray) for the *DLX6* locus, which also encompasses the transcripts *DLX5*, *DLX6-AS1*, and *DLX6-AS2*. **B,** validation of ChIP-Seq data by ChIP-qPCR using specific primers targeting *DLX6*. Blue bars, KNS42; gray, SF188. ***, $P < 0.0001$, *t* test. **C,** boxplot of *DLX6* expression in the integrated pediatric GBM samples stratified by *H3F3A* status. Blue box, G34; green, K27; gray, wild-type. ***, $P < 0.001$, ANOVA. **D,** top, immunohistochemistry for DLX6 protein in a G34 mutant pediatric GBM sample RMH2465. Bottom, barplot of DLX6 expression in a pediatric GBM tissue microarray stratified by *H3F3A* status. Blue bars, G34; green, K27; gray, wild-type. ++, strong expression; +, moderate expression; –, negative. *SOX2:* **E,** ChIP-Seq of H3K36me3 and RNA polymerase II binding for G34-mutant KNS42 (blue) and wild-type SF188 cells (gray) for the *SOX2* locus, which also encompasses the *SOX2-OT* transcript. **F,** validation of ChIP-Seq data by ChIP-qPCR using specific primers targeting *SOX2*. Blue bars, KNS42; gray, SF188. ***, $P < 0.0001$, *t* test. **G,** boxplot of *SOX2* expression in the integrated pediatric GBM samples stratified by *H3F3A* status. Blue box, G34; green, K27; gray, wild-type. *, $P < 0.05$, ANOVA. **H,** top, immunohistochemistry for SOX2 protein in a G34-mutant pediatric GBM sample RMH2465. Bottom, barplot of SOX2 expression in a pediatric GBM tissue microarray stratified by *H3F3A* status. Blue bars, G34; green, K27; gray, wild-type. ++, strong expression; +, moderate expression; –, negative.

differential H3K36me3 and RNA polymerase II binding observed by ChIP-Seq (Fig. 3A) was validated by ChIP-qPCR (Fig. 3B), and expression of *DLX6* was noted to be significantly higher in G34 pediatric GBM samples than K27-mutant or wild-type tumors in the integrated gene expression datasets at the mRNA level (Fig. 3C), and at the protein level in a tissue microarray comprising 46 pediatric and young adult GBM cases (Fig. 3D and Supplementary Table S4). Other similarly validated forebrain development-associated transcription factors included *ARX* (8), *DLX5* (7), *FOXA1* (9), *NR2E1* (10), *POU3F2* (11), and *SP8* (ref. 12; Supplementary Fig. S5–S10). Moreover, a number of key determinants of cell fate were also found to be differentially bound by H3K36me3 and expressed in G34-mutant cells. These included *MSI1* (Musashi-1; ref. 13; Supplementary Fig. S11); *EYA4 (*eyes absent homolog 4; ref. 14; Supplementary Fig. S12); and *SOX2*, which is required for stem cell maintenance (Fig. 3E–H).

Strikingly, the most significant differentially bound and expressed gene in our G34-mutant KNS42 cells was *MYCN* (33-fold H3K36me3 compared with SF188, DESeq $P = 7.94 \times 10^{-8}$; 60-fold RNA Pol II, DESeq $P = 1.59 \times 10^{-9}$; Fig. 4A–D). Of note, a small number of *H3F3A* wild-type tumors also expressed high levels of *MYCN*, and were found to be *MYCN* gene amplified (Fig. 4C). However, amplification was not seen in G34-mutant tumors, which parallels observations in diffuse intrinsic pontine glioma where *MYCN* amplification was found in wild-type, but not K27-mutant, tumors (15). Transduction of the G34V mutation into normal human astrocytes (NHA) and transformed human fetal glial cells (SVG) conferred an approximately 2- to 3-fold increase in *MYCN* transcript levels over wild-type–transduced controls, validating these observations (Supplementary Fig. S13). *H3F3A* G34 mutation may therefore represent an alternative mechanism of enhancing expression levels of MYCN in pediatric GBM.

Targeting MYCN is an attractive therapeutic intervention in tumors harboring gene mutation such as neuroblastoma (16), and direct inhibition by siRNA knockdown in KNS42 cells reduced cell viability in proportion to the reduction of protein levels observed (Fig. 4E). Pharmacologic agents that directly inhibit Myc transcription factors, however, remain elusive. We therefore carried out a synthetic lethal screen to ascertain how we might target these *H3F3A* G34-mutant, MYCN-driven tumors in the clinic. We utilized a series of siRNAs directed against 714 human kinases against our panel of pediatric glioma cell lines to identify those which conferred selective cell death to the MYCN-expressing KNS42 cells versus wild-type, non-MYCN–expressing controls (Fig. 4F). The most significant synthetically lethal hits in the G34-mutant cells compared with *H3F3A* wild-type were kinases

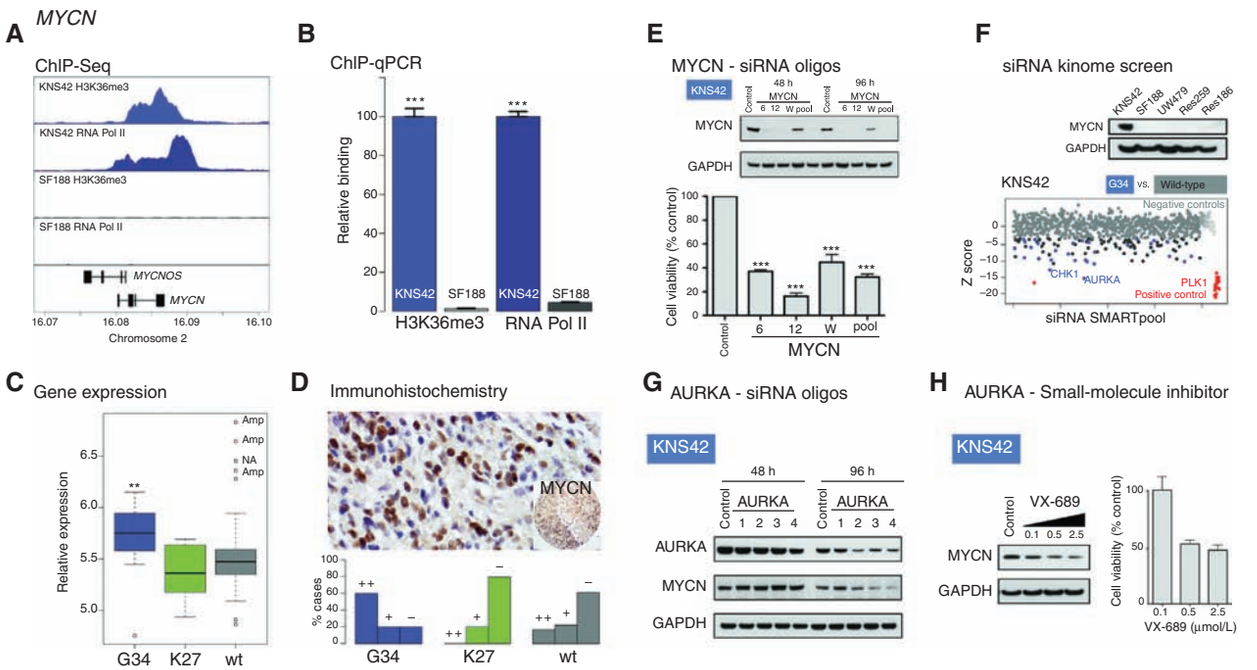

Figure 4. G34 H3K36me3 upregulates MYCN which is selectively targetable by kinases that destabilize the protein. MYCN: **A,** ChIP-Seq of H3K36me3 and RNA polymerase II binding for G34-mutant KNS42 (blue) and wild-type (wt) SF188 cells (gray) for the *MYCN* locus, which also encompasses the *MYCNOS* transcript. **B,** validation of ChIP-Seq data by ChIP-qPCR using specific primers targeting *MYCN*. Blue bars, KNS42; gray, SF188. ***, $P < 0.0001$, *t* test. **C,** boxplot of *MYCN* expression in the integrated pediatric GBM samples stratified by *H3F3A* status. Blue box, G34; green, K27; gray, wild-type. **, $P < 0.01$, ANOVA. Wild-type tumors with high mRNA expression were frequently amplified (Amp). **D,** top, immunohistochemistry for MYCN protein in a G34-mutant pediatric GBM sample. RMH2465 bottom, barplot of MYCN expression in a pediatric GBM tissue microarray stratified by *H3F3A* status. Blue bars, G34; green, K27; gray, wild-type. ++, strong expression; +, moderate expression; −, negative. **E,** effects on cell viability of MYCN knockdown in KNS42 cells. Western blot analysis showing efficiency of reduction of MYCN by 3 individual siRNAs targeting *MYCN* (named 6, 12, and W) and a pool of all 3 after 48 and 96 hours. Barplot showing effects on KNS42 cell viability after siRNA knockdown at 7 days. ***, $P < 0.001$, *t* test versus control. **F,** siRNA screen for 714 human kinases in KNS42 cells. Western blot analysis showing expression of MYCN protein in G34-mutant KNS42 cells in contrast to a panel of wild-type pediatric glioma lines. GAPDH is used as a loading control. Kinase targets are plotted in plate well order along the *x*-axis, and *Z* scores along the *y*-axis. *PLK1* is used as a positive control and is plotted in red. Negative controls are colored light gray, and kinases with *Z* scores greater than −2.0 (no effect on cell viability) are colored gray. "Hits" (*Z* score < −2.0) are colored dark gray or blue, the latter if the effect on cell viability is specific to KNS42 cells and not in a panel of 4 *H3F3A* wild-type pediatric glioma cell lines. The most significant and selective hits were for *CHK1* and *AURKA*. **G,** effect of knockdown of AURKA on MYCN levels in KNS42 cells. Western blot analysis for AURKA and MYCN in KNS42 cells treated with individual oligonucleotides directed against AURKA for 48 and 96 hours. GAPDH is used as a loading control. **H,** effect of a selective small-molecule inhibitor of AURKA on MYCN protein levels and cell viability. Left, Western blot analysis for MYCN protein in KNS42 cells after exposure to 0.1, 0.5, and 2 to 5 μmol/L VX-689 (triangle). GAPDH is used as a loading control. Right, barplot showing effects on cell viability of KNS42 cells exposed to 0.1, 0.5, and 2 to 5 μmol/L VX-689. **, $P < 0.01$, *t* test versus control.

that have been previously associated with stabilization of MYCN protein, specifically *CHK1* (checkpoint kinase 1; ref. 17) and *AURKA* (aurora kinase A; ref. 18). Knockdown of *AURKA* by an independent set of 4 individual oligonucleotides targeting the gene led to a concurrent reduction of MYCN protein in KNS42 cells (Fig. 4G). This destabilization of MYCN was also observed in a dose-dependent manner using a highly selective small-molecule inhibitor of *AURKA*, VX-689 (also known as MK-5108; ref. 19), at concentrations, which in addition led to a significant reduction in viability of the G34-mutant cells (Fig. 4H). Together, these data show the use of targeting MYCN stability in *H3F3A* G34-mutant pediatric GBM as a means of treating this subgroup of patients.

DISCUSSION

Emerging evidence strongly suggests that pediatric GBMs with *H3F3A* mutations can be subclassified into distinct entities. Our data indicate key molecular and clinical differences between G34- and K27-mutant tumors, reflecting the anatomic specificity (K27 tumors restricted to the pons and thalamus and G34 to the cerebral hemispheres; ref. 15; Supplementary Table S4) and likely distinct developmental origins of these disease subgroups. Using the only known model of *H3F3A*-mutant cells to date, we propose that the gene expression signature associated with G34 mutation in pediatric GBM patient samples is likely driven by a genomic differential binding of the transcriptionally activating H3K36me3 mark.

Mapping these gene expression signatures to publicly available datasets of human brain development shows a strong overlap with the ganglionic eminences of the embryonic and early fetal periods. These structures represent a transiently proliferating cell mass of the fetal subventricular zone, are the source of distinct neuroglial progenitors (20), and are therefore strong candidates for the location of the cells of origin of cerebral hemispheric G34-driven pediatric GBM. As with other pediatric brain tumors (21, 22), mutation-driven subgroups of GBM retain gene expression signatures related to discrete cell

populations from which these distinct tumors may arise. In addition, this mutation-driven differential H3K36me3 binding leads to a significant upregulation of numerous genes associated with cell fate decisions. Thus, we have identified a transcriptional readout of the likely developmental origin of G34-mutant GBM coupled with a self-renewal signature we previously identified in KNS42 cells (23) driven by mutation-induced differential binding of H3K36me3.

Significantly, the G34 mutation additionally upregulates MYCN through H3K36me3 binding. It was recently reported that the forced overexpression of stabilized MYCN protein in neural stem cells of the developing mouse forebrain gave rise to GBMs (24), and thus we provide the mechanism by which the initiating tumorigenic insult is delivered at the correct time and place (25) during neurogenesis. Targeting stabilization of MYCN protein via synthetic lethality approaches in *H3F3A* G34-mutant pediatric GBM provides a potential novel means of treating this subgroup of patients.

METHODS

Primary Pediatric Glioblastoma Expression Profiling

Expression data from the Schwartzentruber and colleagues (ref. 2; GSE34824) and Paugh and colleagues (3GSE19578) studies were retrieved from the Gene Expression Omnibus (www.ncbi.nlm.nih.gov/geo/) and analyzed in GenePattern using a signal-to-noise metric, and GSEA implemented for testing of enrichment of gene lists. Pediatric GBM expression signatures were mapped to specific developmental stages and anatomic locations using a spatiotemporal gene expression dataset of human brain development in Kang and colleagues (ref. 6; GSE25219).

Tissue Microarrays

Immunohistochemistry for *DLX6* (NBP1-85929, Novus Biologicals), SOX2 (EPR3131, Epitomics), and MYCN (#9405, Cell Signalling) was carried out on tissue microarrays consisting of 46 cases of pediatric and young adult GBM ascertained for *H3F3A* mutation by Sanger sequencing.

Cell Line Analysis

Pediatric GBM KNS42 cells were obtained from the JCRB (Japan Cancer Research Resources) cell bank. Pediatric SF188 cells were kindly provided by Dr. Daphne Haas-Kogan (University of California San Francisco, San Francisco, CA), whereas UW479, Res259, and Res186 were kindly provided by Dr. Michael Bobola (University of Washington, Seattle, WA). All cells have been extensively characterized previously (4), and were authenticated by short tandem repeat (STR) profiling. Western blot analysis was carried out for total histone H3 (ab97968, Abcam), as well as H3K36 trimethylation (ab9050, Abcam), dimethylation (ab9049, Abcam), and monomethylation (ab9050, Abcam), after histone extraction using a histone purification minikit (ActiveMotif), and quantitated by scanning on the Storm 860 Molecular Imager (GE Healthcare) and analyzed using ImageQuant software (GE Healthcare). Additional Western blots for MYCN (#9405, Cell Signaling), ATRX (sc-15408, Santa Cruz), and glyceraldehyde-3-phosphate dehydrogenase (GAPDH; #2118, Cell Signaling) were carried out according to standard procedures.

Chromatin Immunoprecipitation

Chromatin immunoprecipitation (ChIP) was carried out using antibodies against H3K36me3 and RNA polymerase II using the HistonePath and TranscriptionPath assays by ActiveMotif. Whole genome sequencing was carried out using an Illumina HiSeq2000 instrument with a fold coverage of more than 30 fold. Validation of active regions was carried out by ChIP-quantitative PCR (qPCR).

siRNA Screening and Validation

siRNA screening was carried out on a library of 714 human kinases using Dharmacon SMARTpools (Dharmacon), with cell viability estimated via a highly sensitive luminescent assay measuring cellular ATP levels (CellTiter-Glo; Promega). *Z*-scores were calculated using the median absolute deviation of all effects in each cell line. Individual ON-TARGETplus oligonucleotides for validation were obtained from Dharmacon and knockdown validated by Western blot analysis for *AURKA* (#4718, Cell Signaling) according to standard procedures for up to 96 hours. The *AURKA*-selective small-molecule inhibitor VX-689 (MK-5108) was obtained from Selleckchem and assayed for up to 5 days. Effects on cell viability were assessed by CellTiter-Glo (Promega). siRNAs targeting human MYCN were custom designs and kindly provided by Janet Shipley (Institute of Cancer Research, London, United Kingdom).

Disclosure of Potential Conflicts of Interest

[Q10]

No potential conflicts of interest were disclosed.

Authors' Contributions

[Q11]

Conception and design: D. Hargrave, A. Ashworth, P. Workman, C. Jones

Acquisition of data (provided animals, acquired and managed patients, provided facilities, etc.): L. Bjerke, A. Mackay, M. Nandhabalan, A. Burford, A. Jury, S. Popov, D.A. Bax, D. Carvalho, K.R. Taylor, M. Vinci, I. Bajrami, D. Hargrave, A. Ashworth, P. Workman, C. Jones

Analysis and interpretation of data (e.g., statistical analysis, biostatistics, computational analysis): I.M. McGonnell, D. Hargrave, A. Ashworth, P. Workman, C. Jones

Writing, review, and/or revision of the manuscript: I.M. McGonnell, C.J. Lord, R.M. Reis, D. Hargrave, A. Ashworth, P. Workman, C. Jones

Study supervision: D. Hargrave, A. Ashworth, P. Workman, C. Jones

Acknowledgments

[Q12]

The authors acknowledge NHS funding to the Biomedical Research Centre.

Grant Support

This work is supported by Cancer Research UK, the Wellcome Trust, the Samantha Dickson Brain Tumour Trust, and The Stravros Niarchos Foundation.

Received September 20, 2012; revised January 25, 2013; accepted January 28, 2013; published OnlineFirst ■■■, ■■■.

REFERENCES

1. Jones C, Perryman L, Hargrave D. Paediatric and adult malignant glioma: close relatives or distant cousins? Nat Rev Clin Oncol 2012;9:400–13.
2. Schwartzentruber J, Korshunov A, Liu XY, Jones DT, Pfaff E, Jacob K, et al. Driver mutations in histone H3.3 and chromatin remodelling genes in paediatric glioblastoma. Nature 2012;482:226–31.
3. Paugh BS, Qu C, Jones C, Liu Z, Adamowicz-Brice M, Zhang J, et al. Integrated molecular genetic profiling of pediatric high-grade gliomas reveals key differences with the adult disease. J Clin Oncol 2010;28:3061–8.
4. Bax DA, Mackay A, Little SE, Carvalho D, Viana-Pereira M, Tamber N, et al. Molecular and phenotypic characterisation of paediatric glioma cell lines as models for preclinical drug development. PloS ONE 2009;4:e5209.

5. Wagner EJ, Carpenter PB. Understanding the language of Lys36 methylation at histone H3. Nat Rev Mol Cell Biol 2012;13:115–26.
6. Kang HJ, Kawasawa YI, Cheng F, Zhu Y, Xu X, Li M, et al. Spatio-temporal transcriptome of the human brain. Nature 2011;478:483–9.
7. Panganiban G, Rubenstein JL. Developmental functions of the Distal-less/Dlx homeobox genes. Development 2002;129:4371–86.
8. Kitamura K, Yanazawa M, Sugiyama N, Miura H, Iizuka-Kogo A, Kuaka M, et al. Mutation of ARX causes abnormal development of forebrain and testes in mice and X-linked lissencephaly with abnormal genitalia in humans. Nat Genet 2002;32:359–69.
9. Chatterjee S, Bourque G, Lufkin T. Conserved and non-conserved enhancers direct tissue specific transcription in ancient germ layer specific developmental control genes. BMC Dev Biol 2011;11:63.
10. Monaghan AP, Bock D, Gass P, Schwaeger A, Wolfer DP, Lipp HP, et al. Defective limbic system in mice lacking the tailless gene. Nature 1997;390:515–7.
11. McEvilly RJ, de Diaz MO, Schonemann MD, Hooshmand F, Rosenfeld MG. Transcriptional regulation of cortical neuron migration by POU domain factors. Science 2002;295:1528–32.
12. Zembrzycki A, Griesel G, Stoykova A, Mansouri A. Genetic interplay between the transcription factors Sp8 and Emx2 in the patterning of the forebrain. Neural Dev 2007;2:8.
13. Okano H, Kawahara H, Toriya M, Nakao K, Shibata S, Imai T. Function of RNA-binding protein Musashi-1 in stem cells. Exp Cell Res 2005;306:349–56.
14. Li X, Oghi KA, Zhang J, Krones A, Bush KT, Glass CK, et al. Eya protein phosphatase activity regulates Six1-Dach-Eya transcriptional effects in mammalian organogenesis. Nature 2003;426:247–54.
15. Khuong-Quang DA, Buczkowicz P, Rakopoulos P, Liu XY, Fontebasso AM, Bouffet E, et al. K27M mutation in histone H3.3 defines clinically and biologically distinct subgroups of pediatric diffuse intrinsic pontine gliomas. Acta Neuropathol 2012;124:439–7.
16. Gustafson WC, Weiss WA. Myc proteins as therapeutic targets. Oncogene 2010;29:1249–59.
17. Cole KA, Huggins J, Laquaglia M, Hulderman CE, Russell MR, Bosse K, et al. RNAi screen of the protein kinome identifies checkpoint kinase 1 (CHK1) as a therapeutic target in neuroblastoma. Proc Natl Acad Sci U S A 2011;108:3336–41.
18. Otto T, Horn S, Brockmann M, Eilers U, Schuettrumpf L, Popov N, et al. Stabilization of N-Myc is a critical function of Aurora A in human neuroblastoma. Cancer Cell 2009;15:67–78.
19. Shimomura T, Hasako S, Nakatsuru Y, Mita T, Ichikawa K, Kodera T, et al. MK-5108, a highly selective Aurora-A kinase inhibitor, shows antitumor activity alone and in combination with docetaxel. Mol Cancer Ther 2010;9:157–66.
20. Miyoshi G, Hjerling-Leffler J, Karayannis T, Sousa VH, Butt SJ, Battiste J, et al. Genetic fate mapping reveals that the caudal ganglionic eminence produces a large and diverse population of superficial cortical interneurons. J Neurosci 2010;30:1582–94.
21. Johnson RA, Wright KD, Poppleton H, Mohankumar KM, Finkelstein D, Pounds SB, et al. Cross-species genomics matches driver mutations and cell compartments to model ependymoma. Nature 2010;466:632–6.
22. Gibson P, Tong Y, Robinson G, Thompson MC, Currle DS, Eden C, et al. Subtypes of medulloblastoma have distinct developmental origins. Nature 2010;468:1095–9.
23. Gaspar N, Marshall L, Perryman L, Bax DA, Little SE, Viana-Pereira M, et al. MGMT-independent temozolomide resistance in pediatric glioblastoma cells associated with a PI3-kinase-mediated HOX/stem cell gene signature. Cancer Res 2010;70:9243–52.
24. Swartling FJ, Savov V, Persson AI, Chen J, Hackett CS, Northcott PA, et al. Distinct neural stem cell populations give rise to disparate brain tumors in response to N-MYC. Cancer Cell 2012;21:601–13.
25. Phoenix TN, Gilbertson RJ. There's a time and a place for MYCN. Cancer Cell 2012;21:593–5.

AUTHOR QUERIES

AUTHOR PLEASE ANSWER ALL QUERIES

Q1: Page 1: Per journal style, genes, alleles, loci, and oncogenes are italicized; proteins are roman. Please check throughout to see that the words are styled correctly.

Q2: Page 1: Units of measurement have been changed here and elsewhere in the text from "M" to "Mol/L", and related units, such as "mmol/L" and μmol/L," in figures, legends, and tables in accordance with journal style, derived from the Council of Science Editors Manual for Authors, Editors, and Publishers and the Système international d'unités. Please note if these changes are not acceptable or appropriate in this instance.

Q3: Page 1: Please note that as per AACR, reference citations are not allowed in the "Abstract" and hence have been deleted. Please verify.

Q4: Page 1: Please verify the affiliations and their corresponding author links.

Q5: Page 1: Please verify the corresponding author details.

Q6: Page 2: Please verify that change of "to underpin" to "underpins" is correct.

Q7: Page 3: Please verify the quality/labeling of images included within this article. Thank you.

Q8: Page 3: Please confirm that Schwartzentruber 2012 corresponds with ref. 2 and Paugh 2010 with ref. 3 in the numbered reference list.

Q9: Page 5: Can "qPCR" in "ChIP-qPCR" be defined as "quantitative real-time PCR"?

Q10: Page 7: The conflict-of-interest disclosure statement that appears in the proof incorporates the information from forms completed and signed off on by each individual author. No factual changes can be made to disclosure information at the proof stage. However, typographical errors or misspelling of author names should be noted on the proof and will be corrected before publication. Please note if any such errors need to be corrected. Is the disclosure statement correct?

Q11: Page 7: The contribution(s) of each author are listed in the proof under the heading "Authors' Contributions." These contributions are derived from forms completed and signed off on by each individual author. As the corresponding author, you are permitted to make changes to your own contributions. However, because all authors submit their contributions individually, you are not permitted to make changes in the contributions listed for any other authors. If you feel strongly that an error is being made, then you may ask the author or authors in question to contact us about making the changes. Please note, however, that the manuscript would be held from further processing until this issue is resolved.

Q12: Page 7: Please verify the heading "Acknowledgments" and its text for correctness.

AU: Below is a summary of the name segmentation for the authors according to our records. The First Name and the Surname data will be provided to PubMed when the article is indexed for searching. Please check each name carefully and verify that the First Name and Surname are correct. If a name is not segmented correctly, please write the correct First Name and Surname on this page and return it with your proofs. If no changes are made to this list, we will assume that the names are segmented correctly, and the names will be indexed as is by PubMed and other indexing services.

First Name	Surname
Lynn	Bjerke
Alan	Mackay
Meera	Nandhabalan
Anna	Burford
Alexa	Jury
Sergey	Popov
Dorine	Bax
Diana	Carvalho
Kathryn	Taylor
Maria	Vinci
Ilirjana	Bajrami
Imelda	McGonnell
Christopher	Lord
Rui	Reis
Darren	Hargrave
Alan	Ashworth
Paul	Workman
Chris	Jones